Frequency Domain System Identification of a Small Flying-Wing UAS

Justin J. Matt*
University of Kansas, Lawrence, KS 66045

Steven G. Hagerott†
Bell Textron Inc., Wichita, KS 67202

Benjamin C. Svoboda‡, Harold P. Flanagan§ and Haiyang Chao¶
University of Kansas, Lawrence, KS 66045

This paper focuses on system identification of a small, flying-wing UAS using the frequency response method. A flight test procedure is designed to address the unique challenges encountered when conducting system identification for a small flying-wing UAS with elevon controls. These challenges include increased susceptibility to atmospheric disturbances, limited yaw maneuverability, and visual line-of-sight safety requirements. Frequency sweeps are used as control inputs to excite the longitudinal and lateral-directional dynamics over a designed frequency range. Reduced-order transfer functions are first identified to gain initial information on key dynamics and to provide comparison with different models. Then, decoupled longitudinal and lateral-directional state space models are identified from flight data. The models are validated in the time-domain through comparison with doublet maneuver flight data, showing an excellent fit between the dynamic models and flight data. Finally, nondimensional stability and control derivatives and their confidence intervals are computed from the state space models for comparison with other modeling methods.

Nomenclature

CG	=	center of gravity
ICR	=	instantaneous center of rotation
IMU	=	inertial measurement unit
RMS	=	root mean square
SIMO	=	single-input, multi-output
SISO	=	single-input, single-output
TIC	=	Theil inequality coefficient
a_x, a_y, a_z	=	body x-, y-, and z-axis accelerometer measurements
$\overline{CR}$	=	Cramér-Rao bound percentage
DR	=	subscript for Dutch-roll mode
g	=	gravity constant
$\bar{I}$	=	insensitivity percentage
I_{xx}, I_{yy}, I_{zz}	=	moments of inertia
J	=	cost function value
L, M, N	=	roll, pitch, and yaw moment dimensional stability and control derivatives
p, q, r	=	perturbation roll, pitch, and yaw rates
SP	=	subscript for short-period mode
t	=	time

*M.S. Student, Department of Aerospace Engineering, University of Kansas, justinjmatt@ku.edu
†Associate Tech Fellow, Bell Textron Inc., SHagerott@bellflight.com
‡Undergraduate Student, Department of Aerospace Engineering, University of Kansas, ben.svoboda@ku.edu
§Ph.D. Student, Department of Aerospace Engineering, University of Kansas, h682f304@ku.edu
¶Associate Professor, Department of Aerospace Engineering, University of Kansas, chaohaiyang@ku.edu

$T_{\max}$	=	maximum dynamic period of interest
T_{rec}	=	frequency sweep flight record time
T_s	=	sampling time
u, v, w	=	perturbation x-, y-, and z-body axis velocities
$V_{a_0}, \Theta_0, U_0, W_0$	=	trim airspeed, pitch angle, x- and z-body velocities
X, Y, Z	=	longitudinal, lateral, and vertical force dimensional stability and control derivatives
α, β	=	angle of attack and angle of sideslip
δ_a, δ_e	=	aileron and elevator commands
$\delta_{\text{elevon}_{\text{left}}}, \delta_{\text{elevon}_{\text{right}}}$	=	left and right elevon deflection
ζ, ω_n	=	damping coefficient and natural frequency
τ	=	time delay
ϕ, θ	=	perturbation roll and pitch attitudes

I. Introduction

Unmanned aircraft systems (UAS) have become increasingly important platforms for the research and development of next-generation autonomous aircraft, such as urban-air mobility vehicles or autonomous cargo delivery vehicles. A significant step in the development of these UAS is the identification of dynamic models, which is critical to many research applications such as controller design, state estimator design, turbulence impact analysis, and handling quality analysis.

Many modeling techniques have been developed for manned and unmanned aircraft. Physics-based models can be developed using computational methods or wind-tunnel data, while flight test-based models can be developed through system identification techniques. These techniques include time domain- and frequency domain-based methods, which have been studied extensively in the literature for manned aircraft [1–3]. However, small UAS pose unique challenges in system identification due to their relatively low speed, small size, light weight, and often-uncommon configurations, such as the rudderless flying-wing configuration used in this paper. Yet, flying-wing UAS can also serve as an ideal platform for development, comparison, and validation of different modeling techniques due to their simple aerodynamic shape. As such, it is important to develop a system identification procedure that is tailored to small flying-wing UAS.

Several researchers have worked on the problem of small UAS system identification. Linear dynamic models for conventional, fixed-wing UAS with standard, low-cost sensors were identified in [4–6], following the frequency response method outlined in [1]. On board parameter identification of a fixed-wing UAS was performed in [7]. Nonlinear models were identified using time-domain methods in [8–10]. Lateral-directional dynamic models for a flying-wing UAS were identified in [11, 12]. A tailless UAS with conventional rudders located on two vertical stabilizers was used for system identification in [13]. In [14], a two-step system identification procedure was developed for a small, low-cost, flying-wing UAS using exclusively gyro measurements, focusing on identification of uncertain lateral-directional parameters. In summary, few small UAS dynamic models can be found in the literature that are identified from flight data, especially for a flying-wing UAS with only elevon controls. Identified UAS models that accurately describe the longitudinal and lateral-directional dynamics will be useful for research in many areas such as aerodynamic modeling or controller design. Additionally, due to the unique challenges posed by small UAS and a lack of detailed system identification procedures, performing in-house system identification can be difficult. This points to the need for an easily repeatable procedure tailored to these challenges.

In this paper, a flight data collection and system identification procedure was developed using the frequency response method [1] to address the unique challenges of performing system identification with a small flying-wing UAS. Recommendations for flight test design are made based on our experience. Reduced-order transfer function models and state space models were identified for the KHawk Zephyr3-R UAS. Transfer functions were identified to provide initial parameter estimates and further verification of the identified state space models. Decoupled longitudinal and lateral-directional state space models were identified and verified using time-domain data acquired from doublet maneuvers. Nondimensional stability and control derivatives and associated confidence intervals were computed from the identified state space models for comparison with other modeling methods.

This paper is organized as follows. Section II presents the KHawk UAS research platform and describes the dynamic model structures used for identification. Section III describes the UAS system identification method used in this paper, including flight test design, control input design, and a review of the frequency response method for UAS model identification. Longitudinal and lateral-directional model identification results are presented in Section IV. Section V provides concluding remarks and future directions.

II. UAS Platform and Dynamic Models

A. Flying-wing UAS Platform

The system identification procedure was performed using the KHawk Zephyr3-R UAS, which was developed at the Cooperative Unmanned Systems Laboratory (CUSL) at the University of Kansas. The Zephyr3-R, shown in Fig. 1, is a flying-wing UAS with two elevons and an electric motor as control inputs. The elevons are controlled by mixing the aileron and elevator commands generated by a human pilot or autopilot via Eqs. (1-2), where a positive value indicates deflection of the trailing edge downward.

$$\delta_{\text{elevon}_{\text{left}}} = 0.5(\delta_e + \delta_a) \tag{1}$$

$$\delta_{\text{elevon}_{\text{right}}} = 0.5(\delta_e - \delta_a) \tag{2}$$

The UAS is controlled by a Hex Cube Pixhawk autopilot running ArduPilot open-source firmware. The Hex Cube contains three redundant, internal inertial measurement units (IMUs) and interfaces with peripheral devices for sensing, command-generation, telemetry, and data logging. A GPS receiver and airspeed sensor provide position, inertial velocity, and airspeed measurement. IMU and command signal data was used for system identification and recorded at 100 Hz. Specifications of the KHawk Zephyr3-R are shown in Table 1.

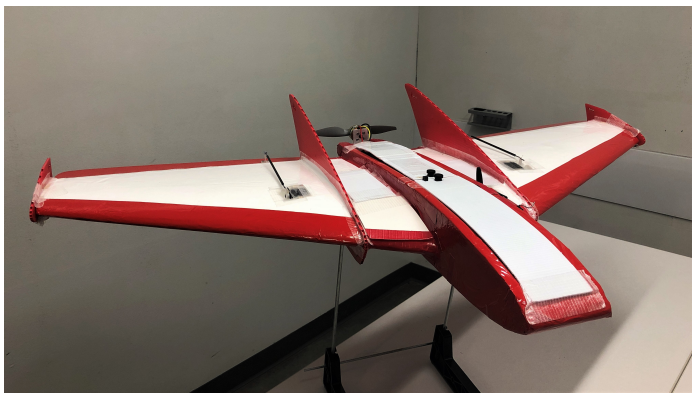

Fig. 1 KHawk Zephyr3-R UAS.

Table 1 Khawk Zephyr3-R UAS specifications.

Mass (kg)	Wingspan (cm)	Cruise Speed (m/s)	Mean Aerodynamic Chord (cm)	Wing Area (m^2)
2.18	122	15-17	31	0.413

B. Aircraft Dynamics

Aircraft dynamics can be described using different dynamic models, including linear single-input, single-output (SISO) models, linear single-input, multi-output (SIMO) models, or nonlinear models. Linearized models are identified in this paper as they provide an accurate representation of UAS dynamics around the trim condition and allow for frequency-domain based analysis. Longitudinal and lateral-directional dynamics are assumed to be decoupled, as is common with fixed-wing aircraft, and identified separately. This section outlines the dynamic models used for system identification.

1. Linear Longitudinal Aircraft Dynamics

The longitudinal aircraft dynamics can be written in state space form, representing a single-input, multi-output (SIMO) model linearized around the trim condition [1]:

$$\begin{bmatrix} \dot{u} \\ \dot{w} \\ \dot{q} \\ \dot{\theta} \end{bmatrix} = \begin{bmatrix} X_u & X_w & X_q - W_0 & -g\cos\Theta_0 \\ Z_u & Z_w & Z_q + U_0 & -g\sin\Theta_0 \\ M_u & M_w & M_q & 0 \\ 0 & 0 & 1 & 0 \end{bmatrix} \begin{bmatrix} u \\ w \\ q \\ \theta \end{bmatrix} + \begin{bmatrix} X_{\delta_e} \\ Z_{\delta_e} \\ M_{\delta_e} \\ 0 \end{bmatrix} \delta_e(t - \tau_{\delta_e}) \tag{3}$$

where u and w are the x-axis and z-axis body velocities, q is the pitch rate, θ is the pitch angle, and δ_e is the elevator command. All states and controls are perturbation values. U_0, W_0, and Θ_0 are the trim x-axis and z-axis body velocities and trim pitch angle, g is the gravity constant, and τ_{δ_e} is the system time delay for elevator inputs. The X, Z, and M terms are the longitudinal dimensional stability and control derivatives to be identified.

Additionally, single-input, single-output (SISO) transfer functions can be used to model the longitudinal dynamics. Simplified, second order transfer functions that describe the q/δ_e, a_z/δ_e, and α/δ_e responses are shown in Eqs. (4-6), where α is the angle of attack (AOA) [15]. When no AOA measurement is available, as is commonly the case for small, low-cost UAS, the response can be modeled from the reconstructed $\dot{w}$ measurement.

$$\frac{q}{\delta_e}(s) = \frac{M_{\delta_e}(s - Z_w)}{s^2 + 2\zeta_{\text{SP}}\omega_{n_{\text{SP}}}s + \omega_{n_{\text{SP}}}^2} e^{-\tau_{\delta_e}s} \tag{4}$$

$$\frac{a_z}{\delta_e}(s) = \frac{K_{az_{\delta e}}}{s^2 + 2\zeta_{\text{SP}}\omega_{n_{\text{SP}}}s + \omega_{n_{\text{SP}}}^2} e^{-\tau_{\delta_e}s} \tag{5}$$

$$\frac{\alpha}{\delta_e}(s) = \frac{1}{sU_0}\frac{\dot{w}}{\delta_e}(s) = \left(\frac{1}{U_0}\right)\frac{Z_{\delta_e}s + (U_0 M_{\delta_e} - Z_{\delta_e}M_q)}{s^2 + 2\zeta_{\text{SP}}\omega_{n_{\text{SP}}}s + \omega_{n_{\text{SP}}}^2} e^{-\tau_{\delta_e}s} \tag{6}$$

where ζ_{SP} and $\omega_{n_{\text{SP}}}$ are the short-period damping and natural frequency.

The SISO models in Eqs. (4-6) omit the phugoid mode dynamics, representing just the short-period mode. As will be discussed in Section III.B.2, Eqs. (4) and (5) often result in errors when estimating the short-period dynamics, and thus the identification procedure must be adapted to prevent these errors. The identified parameters of the SISO models can be used as initial guesses during state space model identification, which can simplify the identification process and provide further verification of the results.

2. Linear Lateral-Directional Aircraft Dynamics

The lateral-directional aircraft dynamics can also be written in state space form, representing a SIMO model linearized around the trim condition [1]:

$$\begin{bmatrix} \dot{v} \\ \dot{p} \\ \dot{r} \\ \dot{\phi} \end{bmatrix} = \begin{bmatrix} Y_v & Y_p + W_0 & Y_r - U_0 & g\cos\Theta_0 \\ L_v & L_p & L_r & 0 \\ N_v & N_p & N_r & 0 \\ 0 & 1 & \tan(\Theta_0) & 0 \end{bmatrix} \begin{bmatrix} v \\ p \\ r \\ \phi \end{bmatrix} + \begin{bmatrix} Y_{\delta_a} \\ L_{\delta_a} \\ N_{\delta_a} \\ 0 \end{bmatrix} \delta_a(t - \tau_{\delta_a}) \tag{7}$$

where v is the y-axis body velocity, p and r are the roll and yaw rates, ϕ is the roll angle, δ_a is the aileron command, and τ_{δ_a} is the system time delay for aileron inputs. All states and controls are perturbation values. The Y, L, and N terms are the lateral-directional dimensional stability and control derivatives to be identified.

Transfer function models can also be used to model the lateral-directional aircraft dynamics. The simplest models assume that the lateral and directional dynamics are decoupled, and are thus reduced to low-order models.

The roll mode is the primary response to aileron, and can be modeled as a first-order transfer function [1]:

$$\frac{p}{\delta_a}(s) = \frac{L_{\delta_a}}{s - L_p} e^{-\tau_{\delta_a}s} \tag{8}$$

The Dutch-roll mode can be identified from the sideslip response, β, which can be modeled from the reconstructed $\dot{v}$ signal [1]:

$$\frac{\beta}{\delta_a}(s) \approx \frac{1}{sU_0}\frac{\dot{v}}{\delta_a} = \frac{K_{\beta_{\delta a}}}{s^2 + 2\zeta_{\text{DR}}\omega_{n_{\text{DR}}}s + \omega_{n_{\text{DR}}}^2} e^{-\tau_{\delta_a}s} \tag{9}$$

where ζ_{DR} and $\omega_{n_{\text{DR}}}$ are the Dutch-roll damping and natural frequency.

These models are simplifications that decouple the lateral and directional controls and dynamics. Furthermore, the sideslip response is usually identified from rudder commands, rather than aileron commands, which causes additional error in the simplification. However, the reduced-order models allow for initial identification of the Dutch-roll mode, roll damping, and roll control gain, which are critical descriptors of the lateral-directional dynamics. These initial estimates will simplify the SIMO identification process and provide useful comparison.

III. Frequency Response Method for UAS System Identification

The objective of the UAS system identification procedure is to determine the model parameters outlined in Section II.B. These models can then be used to design control laws and state estimators. The frequency response method for system identification detailed in [1] is used in this paper. This section outlines the utilization of this method to address the challenges of rudderless flying-wing UAS system identification. This includes control input design, flight procedure design, and a review of the frequency response method.

A. Flight Test Design

Small flying-wing UAS pose unique challenges when designing flight test procedures for system identification. Many of these challenges do not need to be considered for large UAS or manned aircraft, including:

1) Low stability margin for open loop aircraft dynamics due to small flying-wing configuration;
2) Significant impact from wind and atmospheric turbulence due to small size and light weight, which causes disturbances to the aircraft response and makes it difficult to fly at consistent trim conditions
3) Elevon control surfaces lead to increased coupling between the roll and pitch response;
4) No direct yaw control available through elevons;
5) Visual line-of-sight safety requirements which limit the maximum length of system identification maneuvers.

1. Frequency Sweep Design

An important step of the flight test design is determination of the input signal. Input signals should excite the aircraft response uniformly over the desired range of frequencies. In this paper, frequency sweep inputs are used. Key parameters for frequency sweep design include the frequency range, signal magnitude, and record length. For a UAS, these parameters may need to be adjusted for each day or even each flight based on the atmospheric conditions. The frequency range should be selected to excite all rigid body mode frequencies of interest for the UAS. The control signal magnitude, A, should be designed to provide ample signal-to-noise ratio (SNR) without causing responses that depart far from the trim condition. A good rule of thumb is to design the magnitude such that measurements have a SNR greater than three and attitude angles maintain ±10 deg from the trim condition [1]. For a small UAS, we found that attitude variations closer to ±20-25 deg were required for ample SNR and still produced accurate results. Record length, T_{rec}, is directly related to the maximum period, T_{max}, and thus the minimum frequency, that can be identified. Practically, for a small UAS, the record length is recommended to be as long as the pilot can maintain visibility of the aircraft in straight and level flight, as the recommended guideline shown in Eq. (10) [1] cannot always be met. Because of this, low-frequency dynamics may need to be identified using other methods, such as identification from trim data [16].

$$T_{\text{rec}} \geq (4 \text{ to } 5)\, T_{\text{max}} \tag{10}$$

Automated frequency sweeps inputs were programmed in to the autopilot. A discrete-time, exponential frequency sweep is generated by Eqs. (11-14) [1].

$$\delta_{\text{sweep}}[k] = A \sin(\theta_{\text{sweep}}[k]) \tag{11}$$

$$\theta_{\text{sweep}}[k] = \theta_{\text{sweep}}[k-1] + \omega_{\text{sweep}} T_s \tag{12}$$

$$\omega_{\text{sweep}} = \omega_{\text{sweep}_{\text{min}}} + K(\omega_{\text{sweep}_{\text{max}}} - \omega_{\text{sweep}_{\text{min}}}) \tag{13}$$

$$K = 0.0187 e^{4t/T_{\text{rec}}} \tag{14}$$

where A is the signal amplitude, T_s is the sampling time, T_{rec} is the total sweep length, $\omega_{\text{sweep}_{\text{min}}}$ and $\omega_{\text{sweep}_{\text{max}}}$ are the selected minimum and maximum frequencies, t is the current time, and k is the time step index.

The average frequency sweep parameters designed for system identification are shown in Table 2. The frequency range was selected to ensure accurate identification of the key dynamic modes, which can be estimated a priori based on

existing flight data, literature on similar aircraft, or simplified modeling methods. The first period of the sweep was held at constant frequency and the magnitude was faded in to prevent too large of variation in the attitude angle. White noise with a root-mean-square (RMS) level of 10% of the input magnitude was added to the sweep to enrich the spectral content. To suppress high-frequency content, the added white noise should be processed with a low-pass filter with cutoff frequency equal to $\omega_{\text{sweep}_{\text{max}}}$ [1]. The following discrete-time low-pass filter was implemented [17]:

$$y_{\text{LP}}[k] = \alpha_{\text{LP}} y_{\text{LP}}[k-1] + (1-\alpha_{\text{LP}}) u_{LP}[k-1] \tag{15}$$

where

$$\alpha_{\text{LP}} = e^{-a_{\text{LP}} T_s}, \tag{16}$$

a_{LP} is the filter cutoff frequency, T_s is the sampling time, and u_{LP} and y_{LP} are the filter input and output.

Table 2 Average frequency sweep design parameters.

Control	Record Length (s)	Frequency Range (Hz)	Input Magnitude (deg)
δ_e	23	0.5-7	3.0
δ_a	23	0.4-5	2.5-3.5

During automated sweep maneuvers, manual pilot intervention may be required to keep the response near the trim condition, especially at low frequencies. Experimentally, we found that automated sweeps allow the pilot to better focus on keeping the aircraft near the trim condition. Additionally, automated sweeps can be programmed to have different user-configurable settings that can be adjusted during the flight test based on the UAS response. For example, the aileron sweep shown in Figure 2 was programmed to have a smaller magnitude at lower frequencies but a larger magnitude at higher frequencies where the yaw and lateral acceleration responses were heavily attenuated. As such, automated sweeps with the option for additive pilot intervention to help keep the UAS around the trim condition were used for all system identification maneuvers.

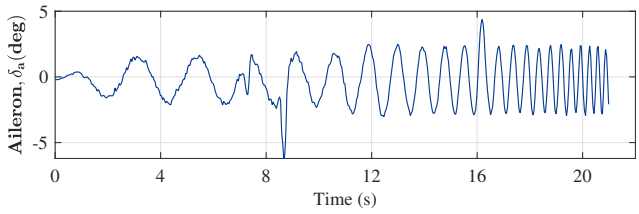

Fig. 2 Automated aileron frequency sweep. The pilot adds corrective inputs around 8s and 16s.

In addition to frequency sweeps, dissimilar inputs should be used for time-domain verification of the identified models to ensure that the model is not over-fitted to the frequency sweep data. In this paper, doublet maneuvers are used for time-domain verification.

2. Flight Test Procedure

The flight test procedure consists of collecting data for frequency-domain system identification and time-domain verification. Many considerations need to be taken during the flight test. Due to the volatility of small UAS to atmospheric turbulence, flight test pilots and engineers should be prepared to adjust the procedure based on observations in the field. Frequency sweep parameters such as record length and input magnitude can vary greatly depending on the visibility and turbulence at the time of flight test. Ideally, flight tests should be performed on calm days.

The following recommendations are made based on those listed in [1] and our flight test experience with small, flying-wing UAS.

- Attempt to maintain trimmed straight and level flight for several seconds before and after the sweep maneuver. This allows for identification of trim parameters and should also be done when performing doublet maneuvers.
- Relaying airspeed and pitch angle information to the pilot via real-time telemetry can help ensure the UAS is operating near the same trim point for all system identification maneuvers, which will lead to a model with improved accuracy. Experimentally, we found that airspeed variation of about ± 2 m/s and roll/pitch variation of about ± 20-25 degrees was sufficient for identifying a highly accurate model.

- The control input magnitude should be adjusted to keep the UAS response symmetric and near the trim point. For automated sweeps, the pilot can intervene if the UAS begins to drift from the trim point.
- The pilot can also maintain the off-axis states at the trim condition, preferably with short, pulsed inputs. For example, during elevator sweeps the aileron should be adjusted to keep the roll angle near zero. For a small UAS, this can be a significant task that is easier to perform during automated sweeps when the pilot does not also have to perform the sweep maneuvers themselves.
- The use of highly-coupled inputs can hinder the system identification process. For a flying-wing UAS, minimizing the number of off-axis inputs required to keep the aircraft at trim will increase the data quality, due to the increased coupling between roll and pitch. Experimentally, we found that engaging the off-axis controller during frequency sweeps resulted in comparatively lower quality data.
- Frequency sweep parameters are suggested to be adjusted based on monitored telemetry data. For example, the sweep magnitude could be adjusted if the SNR of a response was too small. As mentioned, the ideal parameters may change depending on the atmospheric conditions at the time of flight test.
- Flying with a headwind during all maneuvers can improve consistency in trim conditions and allow for an increased record time.

B. UAS Model Identification

1. System Identification using CIFER® Software Package

After flight data was collected, the system identification process was performed using CIFER® (Comprehensive Identification from Frequency Responses), a commercial software package developed by the U.S. Army Aviation Development Directorate [1]. CIFER® consists of several modules that are used for different steps of the system identification process. The FRESPID and COMPOSITE modules are used to estimate SISO frequency responses from flight test data. Estimates are optimized across multiple spectral windows, which decreases random error. NAVFIT is used to fit SISO transfer function models to the estimated frequency responses and identify key parameters that are used as initial guesses when performing state space model identification with the DERIVID model. Lastly, VERIFY is used to validate the state space model in the time domain.

An important feature of the frequency domain method is the presence of several accuracy metrics. The coherence function, γ^2_{xy}, provides an estimate of the accuracy of the non-parametric frequency responses identified in FRESPID and COMPOSITE. Coherence is defined at each discrete frequency by [1]

$$\gamma^2_{xy} = \frac{|\hat{G}^2_{xy}|}{|\hat{G}_{xx}||\hat{G}_{yy}|} \tag{17}$$

where $\hat{G}_{xx}, \hat{G}_{yy}, \hat{G}_{xy}$, are the estimated input, output, and cross spectrums computed using chirp z-transforms.

Coherence ranges from zero to one and measures the linear relationship between the input and output signals in the frequency domain. Typically, a coherence above 0.6 indicates the response at that frequency will have acceptable accuracy. When fitting models to the flight data, a "fitting range" of frequencies should be selected such that the coherence within the range is above 0.5. Within this range, narrow coherence dips are not of concern, as they can be avoided by adjusting the distribution of discrete frequency points. Data at frequencies outside the fitting range will be neglected. Additionally, if any fitting range has a ratio between the maximum and minimum frequencies less than two, the response should not be used in the system identification process [1].

In NAVFIT and DERIVID, parametric models are identified by minimizing the magnitude and phase error between the model and estimated frequency response using a quadratic cost function, J, that is weighted by the coherence at each frequency. The cost function serves as the primary accuracy metric of the identified models. For state space model identification, an average cost value below 100 indicates an accurate model, and an average cost value below 50 reflects a model that is nearly indistinguishable from flight data [1].

Multi-output identification has additional metrics in the Cramér-Rao bound percentage, $\overline{CR}$, and insensitivity percentage, $\bar{I}$. Cramér-Rao bounds measure the level of confidence in the accuracy of an identified parameter, and are scaled by a factor of 2 in CIFER® to more accurately reflect the standard deviation of the parameter [1]. High insensitivity indicates that changes in a parameter has little to no effect on the cost function. For accurately identified parameters, a general guideline using these metrics is [1]:

$$\overline{CR}_i \leq 20\% \tag{18}$$

$$\overline{I_i} \leq 10\% \tag{19}$$

These guidelines are an important part of the model reduction process, which may be necessary to prevent over-parametrized models that result in poor predictive accuracy. In this paper, the iterative reduction process described in [1] was followed, where parameters are dropped, or set to zero, if they do not meet the criteria of Eqs. (18-19) and dropping the term does not result in an excessive increase to the cost functions.

The last step of the system identification procedure is verification of the state space model in the time domain. The VERIFY module is used to compare the model with flight data, while removing biases and references in the data to produce a one-to-one comparison. Doublet maneuvers were collected and used for time domain verification. Theil's inequality coefficient (TIC) is used to represent the overall fit. TIC quantifies the average RMS error as a ratio of the RMS values of the signals. Thus, TIC ranges from 0 to 1, with 0 indicating a perfect fit. A general rule of thumb is that a TIC below 0.25 to 0.30 indicates an accurate fit [1].

2. Transfer Function Models

SISO transfer functions can be identified prior to performing state space model identification as a "sanity check" of critical model parameters. The simplified transfer functions shown in Eqs. (4-6, 8-9) are useful for this purpose.

The short-period assumption made to derive Eqs. (4-5) leads to errors when identifying the short-period dynamics and numerator parameters. Specifically, Z_w in Eq. (4) tends to drift away from its true value, and the a_z/δ_e model is only accurate when the accelerometer measurement is aligned with, or corrected to, the instantaneous center of rotation (ICR) [1]. The latter is particularly problematic for a flying-wing configuration, as the distance between the ICR and accelerometer measurement (located at the CG) will be large due to the short elevon moment arm.

To account for these errors, the q/δ_e and a_z/δ_e response can be fit simultaneously, ensuring that the denominator, or short-period mode, is equivalent for both. This capability is supported in CIFER®. Alternatively, identification of the α/δ_e transfer function in Eq. (6) should provide accurate identification of the short-period dynamics. However, the zero in the numerator of α/δ_e may be above the frequencies that can be identified accurately, resulting in high cost. As such, the zero was neglected, and α/δ_e was identified using a standard second order transfer function of the form in Eq. (20).

$$\frac{\alpha}{\delta_e} = \frac{1}{U_0} \frac{K_{\alpha_{\delta e}}}{s^2 + 2\zeta_{\mathrm{SP}}\omega_{n_{\mathrm{SP}}} s + \omega_{n_{\mathrm{SP}}}^2} e^{-\tau_{\delta_e} s} \tag{20}$$

Approximations can be made to relate the short-period frequency to state space model parameters [18]:

$$\omega_{n_{\mathrm{SP}}}^2 \approx \frac{Z_\alpha M_q}{U_0} - M_\alpha \tag{21}$$

Typically, $M_\alpha \gg Z_\alpha M_q / U_0$. Thus,

$$\omega_{n_{\mathrm{SP}}}^2 \approx -M_\alpha \approx -M_w U_0 \tag{22}$$

A similar approximation can be made with the Dutch-roll frequency [18]:

$$\omega_{n_{\mathrm{DR}}}^2 \approx N_\beta + \frac{Y_\beta N_r - N_\beta Y_r}{U_0} \tag{23}$$

$$\omega_{n_{\mathrm{DR}}}^2 \approx N_\beta \approx N_v U_0 \tag{24}$$

Identification of these SISO models, and subsequent parameters, can provide reasonable initial guesses during SIMO identification, which reduces the efforts required. Additionally, comparison between SISO- and SIMO-identified parameters provides a simple and useful verification step.

3. State Space Models

The general SIMO system setup comprises of the equations of motion written in matrix form:

$$\boldsymbol{M\dot{x} = Fx + Gu} \tag{25}$$

where $\boldsymbol{x}$ and $\boldsymbol{u}$ are the system states and controls and $\boldsymbol{M, F, G}$ are the inertial and augmented state space matrices. The measurements, or outputs, $\boldsymbol{y}$, can then be expressed in matrix form as a function of the system states:

$$\boldsymbol{y = H_0 x + H_1 \dot{x}} \tag{26}$$

The form of Eqs. (25-26) is convenient because it allows for the separation of mass matrix terms and simple formulation of accelerometer equations. The equations can also be expressed in standard state space form [1]:

$$\dot{\boldsymbol{x}} = \boldsymbol{A}\boldsymbol{x} + \boldsymbol{B}\boldsymbol{u} \tag{27}$$

$$\boldsymbol{y} = \boldsymbol{C}\boldsymbol{x} + \boldsymbol{D}\boldsymbol{u} \tag{28}$$

where $\boldsymbol{A} = \boldsymbol{M}^{-1}\boldsymbol{F}, \boldsymbol{B} = \boldsymbol{M}^{-1}\boldsymbol{G}, \boldsymbol{C} = \boldsymbol{H}_0 + \boldsymbol{H}_1\boldsymbol{M}^{-1}\boldsymbol{F},$ and $\boldsymbol{D} = \boldsymbol{H}_1\boldsymbol{M}^{-1}\boldsymbol{G}$.

The outputs used for longitudinal and lateral-directional model identification are $(a_x, a_z, q, \dot{u}, \dot{w})$ and $(a_y, p, r, \dot{v})$, where (a_x, a_y, a_z) are the body x-, y-, and z-axis accelerometer measurements recorded by the IMU. The perturbation velocity derivatives, $(\dot{u}, \dot{v}, \dot{w})$, are reconstructed from other measurements. Note that it is necessary to check the kinematic consistency of the attitude angle measurements prior to reconstructing these signals, as described in [1].

$$\dot{u} = a_x - W_0 q - (g\cos\Theta_0)\theta \tag{29}$$

$$\dot{v} = a_y - U_0 r + W_0 p + (g\cos\Theta_0)\phi \tag{30}$$

$$\dot{w} = a_z + U_0 q - (g\sin\Theta_0)\theta \tag{31}$$

The output equations for the longitudinal and lateral-directional systems can then be written as

$$\begin{bmatrix} a_x \\ a_z \\ q \\ \dot{u} \\ \dot{w} \end{bmatrix} = \begin{bmatrix} 0 & 0 & W_0 & g\cos\Theta_0 \\ 0 & 0 & -U_0 & g\sin\Theta_0 \\ 0 & 0 & 1 & 0 \\ 0 & 0 & 0 & 0 \\ 0 & 0 & 0 & 0 \end{bmatrix} \begin{bmatrix} u \\ w \\ q \\ \theta \end{bmatrix} + \begin{bmatrix} 1 & 0 & z_{\text{IMU}} & 0 \\ 0 & 1 & -x_{\text{IMU}} & 0 \\ 0 & 0 & 0 & 0 \\ 1 & 0 & z_{\text{IMU}} & 0 \\ 0 & 1 & -x_{\text{IMU}} & 0 \end{bmatrix} \begin{bmatrix} \dot{u} \\ \dot{w} \\ \dot{q} \\ \dot{\theta} \end{bmatrix} \tag{32}$$

$$\begin{bmatrix} a_y \\ p \\ r \\ \dot{v} \end{bmatrix} = \begin{bmatrix} 0 & -W_0 & U_0 & -g\cos\Theta_0 \\ 0 & 1 & 0 & 0 \\ 0 & 0 & 1 & 0 \\ 0 & 0 & 0 & 0 \end{bmatrix} \begin{bmatrix} v \\ p \\ r \\ \phi \end{bmatrix} + \begin{bmatrix} 1 & -z_{\text{IMU}} & x_{\text{IMU}} & 0 \\ 0 & 0 & 0 & 0 \\ 0 & 0 & 0 & 0 \\ 1 & -z_{\text{IMU}} & x_{\text{IMU}} & 0 \end{bmatrix} \begin{bmatrix} \dot{v} \\ \dot{p} \\ \dot{r} \\ \dot{\phi} \end{bmatrix} \tag{33}$$

where x_{IMU} and z_{IMU} are the positional offsets between the CG of the UAS and the IMU, which is located within the UAS autopilot. For the UAS used in this paper, this offset is approximated to be zero.

IV. UAS System Identification Results

This section presents the UAS system identification results. Non-parametric models were generated from concatenated flight data using CIFER®, then fit to reduced-order transfer function and state space models. Doublet maneuvers were used for time-domain verification, as they provide insight to the model's ability to predict the response of inputs dissimilar to those used for identification.

Steady state conditions were identified by averaging the measurements of data prior to and during system identification maneuvers. For a small UAS, trim conditions can vary significantly, which presents a nontrivial challenge during flight tests. Ensuring that each data set used for identification was performed near the same trim condition will improve the accuracy of the identified models. As a reference, the flight data used for system identification in this paper varied from the trim airspeed by ±2 m/s on average and still produced accurate results. The steady state conditions for the KHawk Zephyr3-R are shown in Table 3. The small difference in trim conditions between the two models is likely a result of flight data collected at different wind conditions on different days. Ideally, each model would be identified at the same trim condition.

Table 3 Zephyr3-R steady state conditions.

Model	U_0 (m/s)	Θ_0 (deg)	W_0 (m/s)
Longitudinal	17	3	0.9
Lateral-directional	15	5	1.3

A. Longitudinal Model Identification

The longitudinal model was acquired from four frequency sweep data sets that were selected based on the desired data specifications discussed in Section III.A. The time-history data of one sweep is shown in Fig. 3. The primary responses have ample SNR for the majority of the maneuver. The aileron history shows the pilot's corrective inputs to attempt to maintain the roll angle at zero. During the maneuver, the roll and pitch angles stays within ±20 degrees and the airspeed varies within ±2 m/s, which was also found to be sufficient for accurate results.

Frequency responses for the longitudinal outputs and the reconstructed AOA signal were computed, and are shown in Fig. 4. Prior to SIMO identification, the transfer functions in Eqs. (4-5, 20) were identified to provide initial insight into the longitudinal dynamics, which are also depicted in Fig. 4. The parameter identification results are shown in Table 4. Corresponding state space model results, which will be discussed in the following, are included for comparison. The q/δ_e and a_z/δ_e transfer functions were fit simultaneously to prevent error in the identification. Each of the transfer functions fit the flight data accurately, as indicated by the low cost function values. The transfer function parameters match closely with the state space model results, providing initial estimates for the state space identification process and a useful "sanity check" of the results. There is a large error in the M_w estimate, which is caused by the approximation that $M_\alpha \gg Z_\alpha M_q/U_0$ used to derive Eq. (22), which is less accurate for a small UAS as U_0 is small. This can be verified using state space parameters to calculate $\omega_{n_{SP}}$ with Eqs. (21-22) and comparing the results.

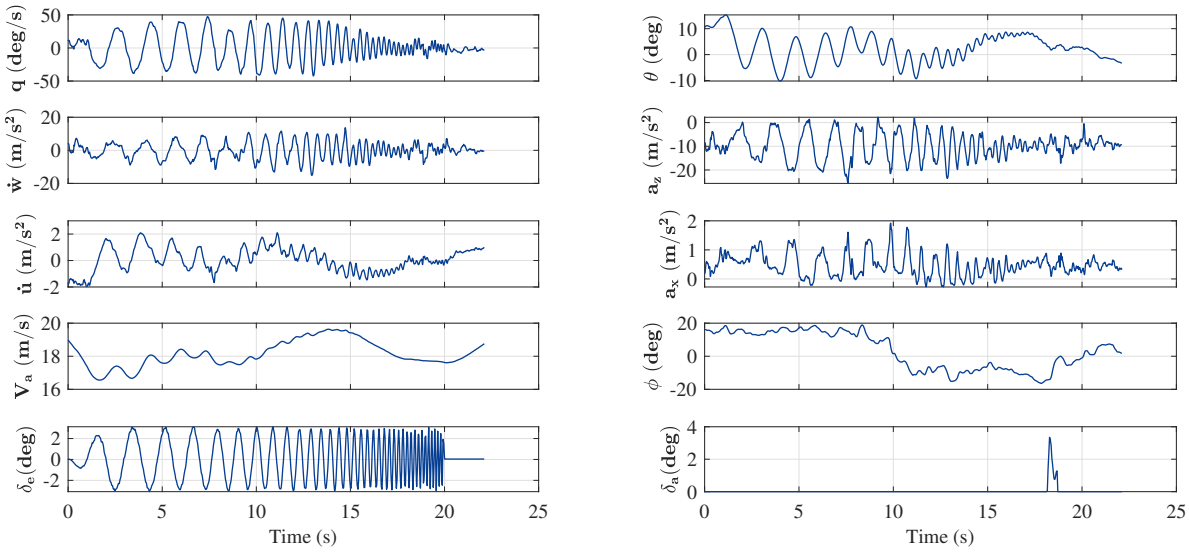

Fig. 3 Time history data of elevator sweep.

Table 4 Longitudinal transfer function parameters.

Parameter	Unit	q/δ_e and a_z/δ_e (Simultaneous Fit)	α/δ_e	State Space Model	Percent Difference (%)
$\omega_{n_{SP}}$	rad/s	8.26	7.99	8.15	1.4, 2.0
ζ_{SP}	-	0.70	0.70	0.66	6.1, 6.1
τ_{δ_e}	s	0.063	0.050	0.060	5.0, 17
M_{δ_e}	s^{-2}	-106	-	-101	5.0
Z_w	s^{-1}	-7.37	-	-7.55	2.4
M_w	$(m\ s)^{-1}$	-4.26	-4.18	-2.47	72, 69
Cost	-	J_q = 11.9, J_{a_z} = 22.6	5.4	J_q = 11.4, J_{a_z} = 23.0	-

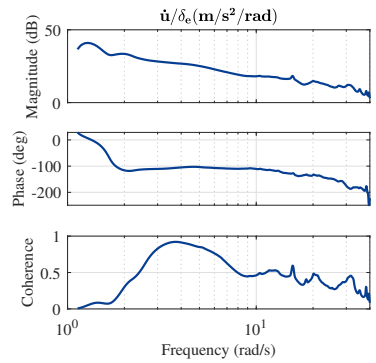

(a) Derivative of x-axis body velocity frequency response.

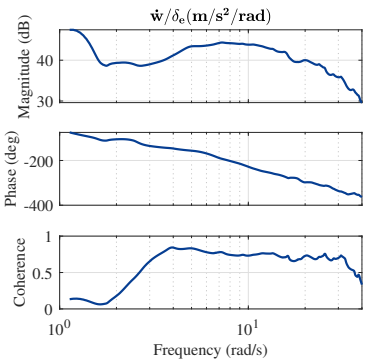

(b) Derivative of z-axis body velocity frequency response.

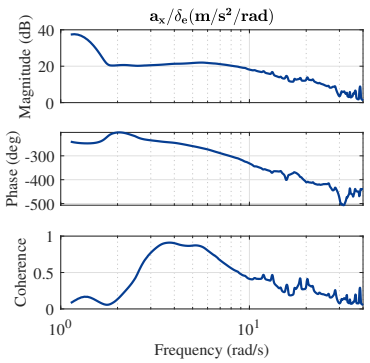

(c) Longitudinal acceleration frequency response.

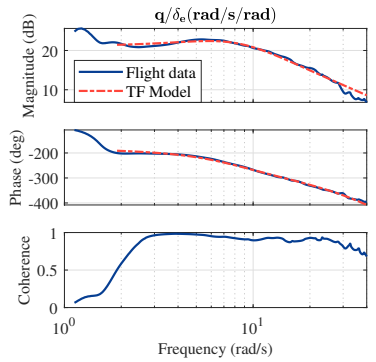

(d) Pitch rate frequency response and transfer function fit (J_q = 11.9).

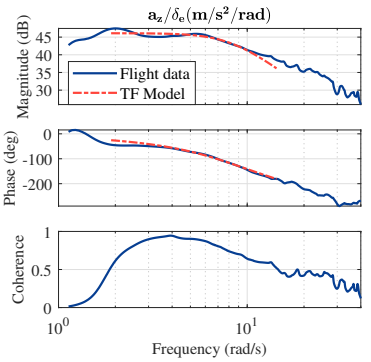

(e) Vertical acceleration frequency response and transfer function fit (J_{a_z} = 22.6).

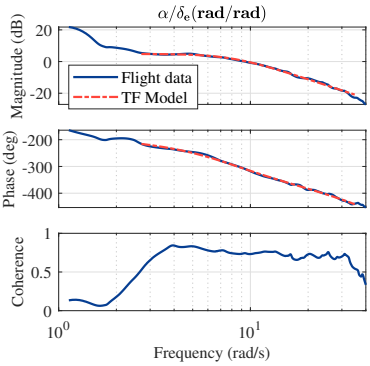

(f) AOA frequency response and transfer function fit. approximated from $\dot{w}$ ($J_{\dot{w}}$ = 5.4).

Fig. 4 Longitudinal frequency responses and transfer function fits.

Table 5 Longitudinal state space model identification results.

Parameter	Unit	Value	Cramér-Rao %	Insensitivity %
X_u	s^{-1}	-0.2776	40.9	14.8
X_w	s^{-1}	0.6201	8.2	1.4
X_q	m/s	-0.3484	25.1	5.0
Z_w	s^{-1}	-7.554	5.6	1.4
M_w	$(m\ s)^{-1}$	-2.465	10.3	1.9
M_q	s^{-1}	-3.252	22.1	2.7
Z_{δ_e}	m/s^2	-21.77	27.5	9.2
M_{δ_e}	s^{-2}	-100.9	4.9	1.0
τ_{δ_a}	s	0.06044	4.2	1.7

Response	Cost Value
a_x/δ_e	3.4
a_z/δ_e	23.0
q/δ_e	11.4
$\dot{u}/\delta_e$	23.0
$\dot{w}/\delta_e$	8.6
Average	13.9

Z_q, X_{δ_e}, M_u, and Z_u were dropped during model identification

Next, SIMO model identification was performed. As discussed, fitting ranges for each transfer function were selected based on a coherence threshold of 0.5. The identified parameters are shown in Table 5. Several parameters were dropped following the iterative process detailed prior, and, as such, the phugoid dynamics are not fully identified. Both the overall and individual cost functions indicate an excellent fit, with all values less than 25. The X_u term has poor accuracy metrics, but was not dropped as it has a significant impact on the a_x and $\dot{u}$ models. All other parameters meet insensitivity guidelines, and just two other parameters, M_q and Z_{δ_e}, exceed the Cramér-Rao guideline, though not significantly. The identification results are compared to the frequency responses from flight data in Fig. 5.

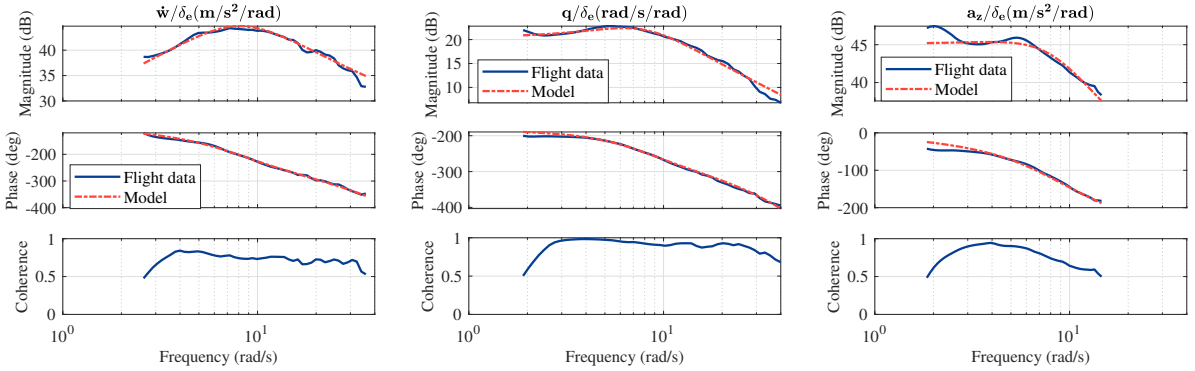

(a) Z-axis body velocity derivative model fit ($J_{\dot{w}}$ = 8.6).

(b) Pitch rate model fit (J_q = 11.4).

(c) Vertical acceleration model fit (J_{a_z} = 23.0).

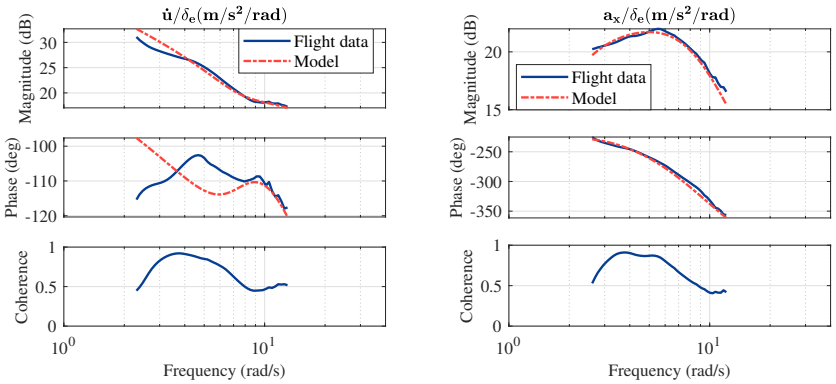

(d) X-axis body velocity derivative model fit ($J_{\dot{u}}$ = 23.0).

(e) Longitudinal acceleration model fit (J_{a_x} = 3.4).

Fig. 5 Longitudinal state space model fit (J = 13.9)

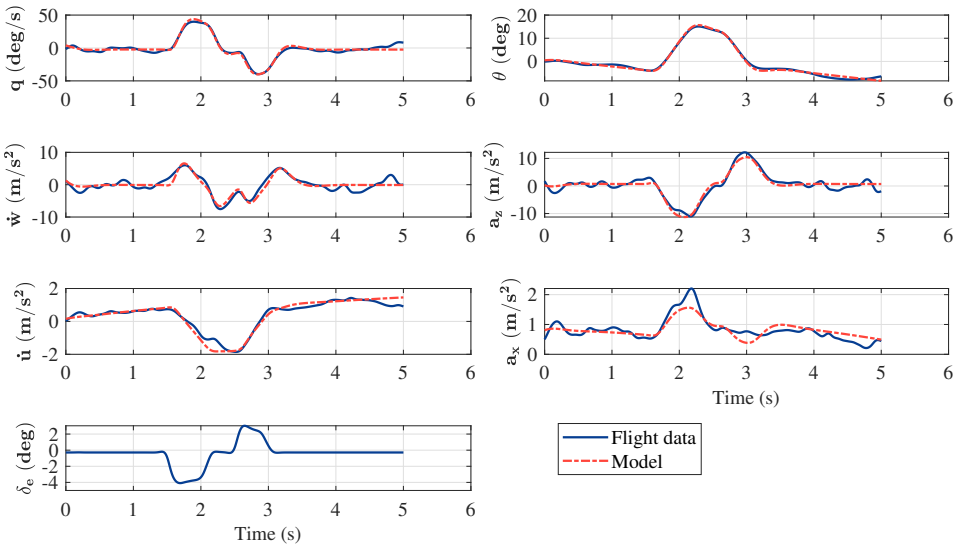

Fig. 6 Time-domain comparison between longitudinal model and flight test data (TIC = 0.09).

The model was validated using time-domain data collected during an elevator doublet maneuver, which is shown in Fig. 6. The model predicts the response very accurately, and much of the error can be attributed to the presence of noise and disturbances in the flight data. The a_x response is the least accurate, which can likely be attributed to the many related parameters that were dropped. The TIC for this fit is 0.09, which indicates a model with high predictive accuracy.

B. Lateral-Directional Model Identification

The lateral-directional model was identified from three frequency sweep data sets. The time-history data of one sweep is shown in Fig. 7. The main challenge when performing aileron sweep maneuvers was ensuring the directional responses have ample SNR across a wide range of frequencies, as the Zephyr3-R has no direct yaw control. The r, a_y, and $\dot{v}$ responses can be clouded by the lightly damped Dutch-roll mode, which is easily excited by even very light wind. This can lead to poor coherence in the frequency responses. This effect can be seen at the very end of the flight record shown in Fig. 7. Generally, we found the best way to combat this is by increasing the magnitude of the aileron input or flying on a calmer day, each of which will serve to improve the SNR. However, it should also be considered that large aileron inputs will result in large roll rates and angles, which could also reduce the identification accuracy if the aircraft departs excessively from the trim point. Thus, it is important to find a good trade-off between SNR and operation near the trim condition.

Lateral-directional frequency response estimates are shown in Fig. 8. The responses have acceptable coherence over a wide range of frequencies. The directional responses all exhibit a dip in coherence near the Dutch-roll frequency. This is likely caused by the wind exciting the Dutch-roll mode during flight, which reduces the SNR of the directional response. This will have an increased impact on the identification process when there are not rudder inputs, which will typically better excite the Dutch-roll mode. Nonetheless, the coherence drop spans a narrow frequency range and reaches a minimum value of 0.5, and thus did not hinder the identification results significantly.

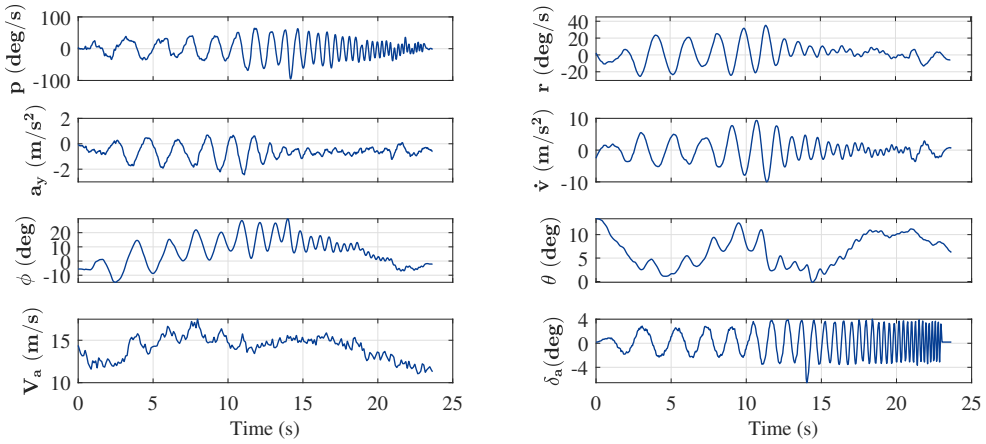

Fig. 7 Aileron sweep time history data.

Table 6 Lateral-directional transfer function parameters.

Parameter	Unit	p/δ_a	β/δ_a	State Space Model	Percent Difference (%)
$\omega_{n_{\text{DR}}}$	rad/s	-	3.48	3.98	13
ζ_{DR}	-	-	0.30	0.31	3.2
τ_{δ_a}	s	0.063	0.065	0.055	15, 18
N_v	$(\text{m s})^{-1}$	-	0.805	0.835	3.6
L_{δ_a}	s^{-2}	186	-	170	10
L_p	s^{-1}	-11.0	-	-8.52	29
Cost	-	24.0	59.4	$J_p = 11.7$ $J_{\dot{v}} = 27.3$	-

Also shown in Fig. 8 are the low-order transfer functions that were fit to the aileron-to-roll-rate and aileron-to-sideslip responses. As with the longitudinal model, these transfer functions provide useful information on dynamic modes and key parameters that simplify the state space model identification process. The parameter identification results are shown in Table 6. Corresponding state space model results, which will be discussed following, are included for comparison. The cost functions indicate accurate models, and the identified parameters match well with the state space model.

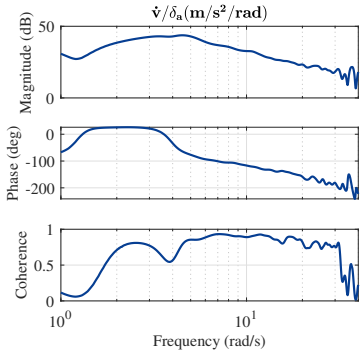

(a) Derivative of y-axis body velocity frequency response.

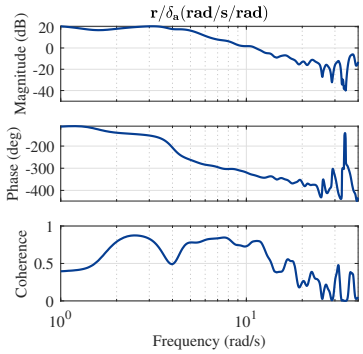

(b) Yaw rate velocity frequency response.

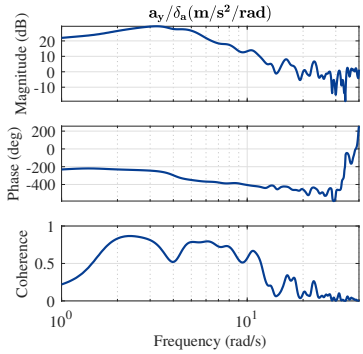

(c) Lateral acceleration frequency response.

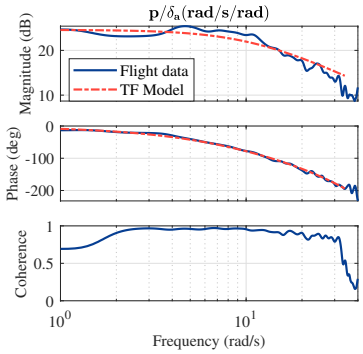

(d) Roll rate frequency response and transfer function fit (J_p = 24.0).

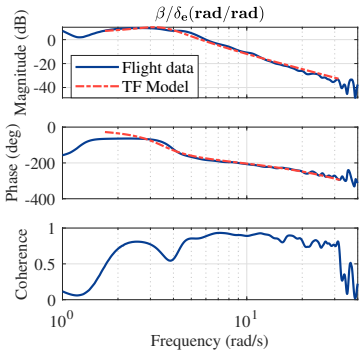

(e) Sideslip frequency response and transfer function fit (J_β = 59.4).

Fig. 8 Lateral-directional frequency responses and transfer function fits.

Table 7 Lateral-directional state space model identification results.

Parameter	Unit	Value	Cramér-Rao %	Insensitivity %		Response	Cost Value
Y_v	s^{-1}	-0.6819	6.3	2.6		$\dot{v}/\delta_a$	27.3
Y_p	m/s	0.1647	22.7	9.8		p/δ_a	11.7
Y_r	m/s	0.5972	33.5	13.4		r/δ_a	29.6
L_v	$(m\ s)^{-1}$	-0.8599	29.2	8.7		a_y/δ_a	17.1
L_p	s^{-1}	-8.517	8.8	1.5		Average	21.4
L_r	s^{-1}	3.144	34.7	9.8		*Y_{δ_a} and N_{δ_a} were dropped during model identification*	
N_v	$(m\ s)^{-1}$	0.8346	5.5	1.6			
N_p	s^{-1}	-0.7113	9.0	2.5			
N_r	s^{-1}	-1.465	13.9	4.0			
L_{δ_a}	s^{-2}	169.7	5.6	1.1			
τ_{δ_e}	s	0.05486	5.7	2.1			

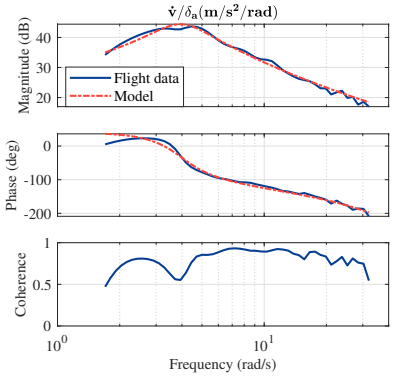

(a) Y-axis body velocity derivative model fit ($J_{\dot{v}}$ = 27.3)

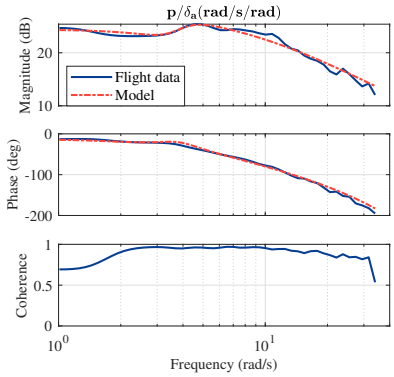

(b) Roll rate model fit (J_p = 11.7)

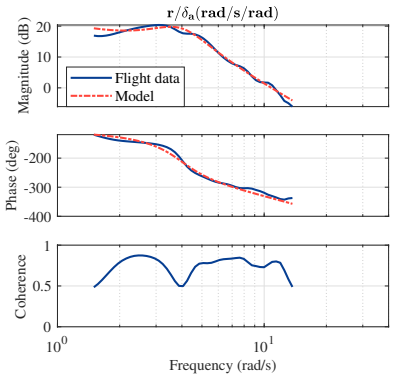

(c) Yaw rate model fit (J_r = 29.6)

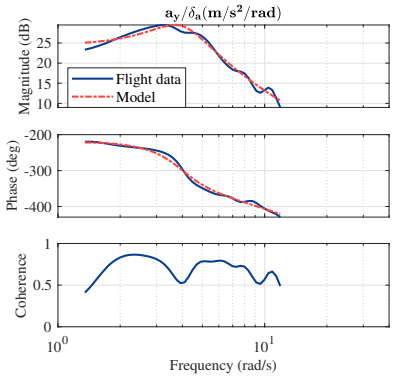

(d) Lateral acceleration model fit (J_{a_y} = 17.1).

Fig. 9 Lateral-directional state space model fit (J = 21.4)

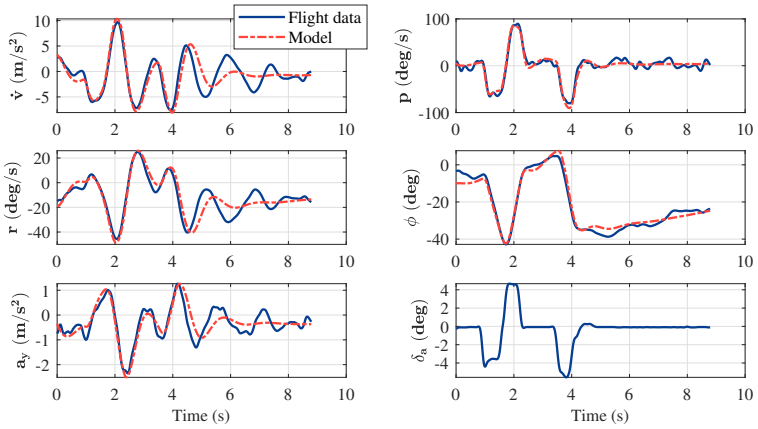

Fig. 10 Time-domain comparison between lateral-directional model and flight test data (TIC = 0.11).

Next, the state space model was fit to the lateral-directional responses. The identified parameters are shown in Table 7. The control derivatives Y_{δ_a} and N_{δ_a} were dropped from the model structure, and set to zero. Both the overall and individual cost functions indicate an excellent fit, with all values less than 30. Just one parameter, Y_r, exceeds the insensitivity guideline, but several parameters exceed the Cramér-Rao guideline. It is likely that these errors are a result of the coherence drop near the Dutch-roll mode. Comparison between the model and flight data is shown in Fig. 9.

The model was validated with data that was collected during an aileron doublet maneuver, followed by a large bank maneuver, shown in Fig. 10. The roll rate and roll angle are predicted accurately for the entirety of the maneuver. The directional responses are predicted accurately in the transient stage of the maneuver, but show error in the settling stage. This is likely caused by variance from the trim airspeed, as the average airspeed during this maneuver was 19 m/s. As a result, the model over-predicts the Dutch-roll damping and exhibits phase lag. Still, the model indicates good predictive accuracy even during a maneuver with very large angular rates. The TIC is 0.11, which indicates an excellent fit.

C. Nondimensional Stability and Control Derivatives

Nondimensional stability and control derivatives were calculated from the state space models, using equations from [15]. The computation of the nondimensional derivatives is a combination of multiple variables that each have their own associated uncertainty. This includes the dimensional derivatives, steady state conditions (which are particularly uncertain for a small UAS), and moment of inertia terms which were estimated using the compound pendulum method [19]. As such, the uncertainties of the nondimensional derivatives must be estimated, as they cannot be computed directly. Identification of these parameters and uncertainties is useful for comparison with other methods, such as wind-tunnel testing or numerical methods, where the nondimensional form of the derivatives may be more useful.

The uncertainties of the nondimensional derivatives were estimated using Monte Carlo simulation. Each of the uncertain variables used in computation of the nondimensional derivatives was simulated as a Gaussian random variable (GRV), with statistics listed in Tables 8 and 9. Variables not listed in the tables, such as mass and geometric properties, are assumed to be known exactly, and thus are not simulated as GRVs. For the dimensional derivatives, the uncertainty is represented by the Cramér-Rao bound, which has been scaled by 2 to represent the standard deviation, as mentioned in Section III.B.1. The standard deviation of the other GRVs is computed from experimental data.

Table 8 Longitudinal random variable statistics.

	U_0 (m/s)	Θ_0 (deg)	I_{yy} (kg m^2)	Dimensional derivatives
Nominal value	17	3	0.126	Identified value
Standard deviation	1.5	1.5	0.008	$\overline{CR}$

Table 9 Lateral-directional random variables statistics.

	U_0 (m/s)	Θ_0 (deg)	I_{xx} (kg m^2)	I_{zz} (kg m^2)	Dimensional derivatives
Nominal value	15	5	0.158	0.217	Identified value
Standard deviation	1.5	1.5	0.009	0.013	$\overline{CR}$

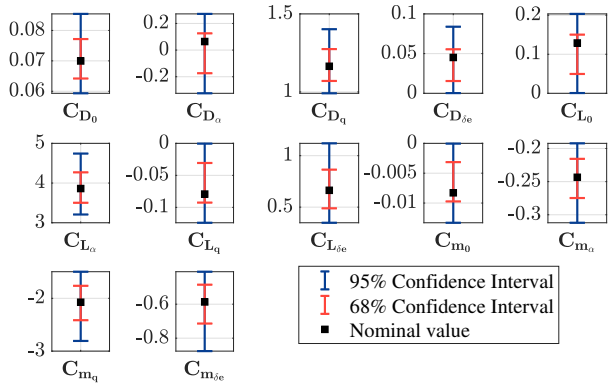

Fig. 11 Longitudinal nondimensional stability and control derivatives.

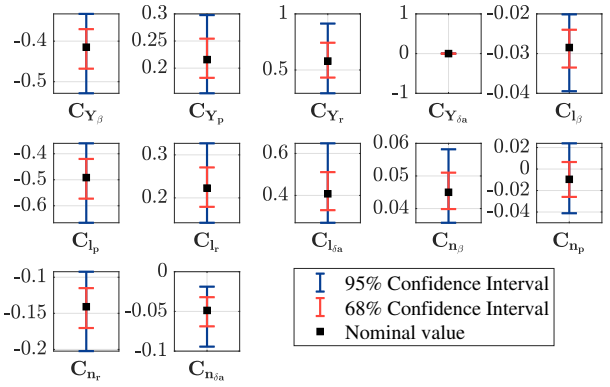

Fig. 12 Lateral-directional nondimensional stability and control derivatives.

A convergence study was performed to determine the number of iterations needed to accurately estimate the confidence intervals. For all derivatives, the probability density function remained relatively constant after 5000 iterations. The nominal value, 68th percentiles, and 95th percentiles were then computed from the converged probability density function. The nondimensional derivatives and associated confidence intervals are shown in Fig. 11-12, and listed fully in Tables 10-11.

The estimated confidence intervals can provide a sense of which nondimensional derivatives were identified most accurately. The longitudinal derivatives most related to the short-period mode (i.e. $C_{L_\alpha}, C_{m_\alpha}, C_{m_q}, C_{L_{\delta e}}$, and $C_{m_{\delta e}}$) have lower uncertainty, while the parameters related to the phugoid mode have higher uncertainty. This matches with the state space model results, as the phugoid dynamics were not fully identified. For the lateral-directional model, all of the derivatives except C_{n_p} exhibit relatively low uncertainty, indicating the accuracy of the identified state space model. C_{n_p} is largely related to Dutch-roll damping and is typically negative in value, becoming closer to zero as the damping decreases [15]. Thus, the light damping of the Dutch-roll mode of this UAS could be a cause of the high uncertainty of this term.

Table 10 Longitudinal nondimensional stability and control derivatives.

Parameter	Lower Bound (95% Confidence)	Lower Bound (68% Confidence)	Nominal Value	Upper Bound (68% Confidence)	Upper Bound (95% Confidence)
$\mathbf{C_{D_0}}$	0.0131	0.041	0.0689	0.1004	0.1318
$\mathbf{C_{D_\alpha}}$	-0.321	-0.1721	-0.0245	0.1276	0.2759
$\mathbf{C_{D_q}}$	0.5859	0.8629	1.1655	1.482	1.8195
$\mathbf{C_{D_{\delta e}}}$	0.0011	0.0150	0.0348	0.0566	0.0866
$\mathbf{C_{L_0}}$	0.0034	0.0501	0.0993	0.1515	0.2051
$\mathbf{C_{L_\alpha}}$	3.1973	3.5007	3.8652	4.2690	4.7691
$\mathbf{C_{L_q}}$	-0.1409	-0.0963	-0.0611	-0.0275	-0.0020
$\mathbf{C_{L_{\delta e}}}$	0.2919	0.4586	0.6640	0.8938	1.1812
$\mathbf{C_{m_0}}$	-0.0136	-0.0098	-0.0064	-0.0032	-0.0002
$\mathbf{C_{m_\alpha}}$	-0.3234	-0.2811	-0.2437	-0.2092	-0.1810
$\mathbf{C_{m_q}}$	-3.1588	-2.5978	-2.074	-1.579	-1.1493
$\mathbf{C_{m_{\delta e}}}$	-0.8776	-0.7114	-0.5867	-0.4872	-0.4119

Table 11 Lateral-directional nondimensional stability and control derivatives.

Parameter	Lower Bound (95% Confidence)	Lower Bound (68% Confidence)	Nominal Value	Upper Bound (68% Confidence)	Upper Bound (95% Confidence)
$\mathbf{C_{y_\beta}}$	-0.5203	-0.4588	-0.4063	-0.3635	-0.3264
$\mathbf{C_{y_p}}$	0.1251	0.1657	0.2112	0.2613	0.3181
$\mathbf{C_{y_r}}$	0.1880	0.3735	0.5675	0.7769	1.0021
$\mathbf{C_{y_{\delta a}}}$	-	-	0	-	-
$\mathbf{C_{l_\beta}}$	-0.0493	-0.0383	-0.0285	-0.0192	-0.0105
$\mathbf{C_{l_p}}$	-0.6598	-0.5689	-0.4917	-0.4234	-0.3637
$\mathbf{C_{l_r}}$	0.0946	0.1556	0.2227	0.2962	0.3766
$\mathbf{C_{l_{\delta a}}}$	0.2733	0.3314	0.4078	0.5087	0.6441
$\mathbf{C_{n_\beta}}$	0.0350	0.0395	0.0450	0.0513	0.0587
$\mathbf{C_{n_p}}$	-0.0437	-0.0265	-0.0096	0.0070	0.0248
$\mathbf{C_{n_r}}$	-0.1931	-0.1655	-0.1409	-0.1204	-0.1034
$\mathbf{C_{n_{\delta a}}}$	-0.0938	-0.0683	-0.0488	-0.0321	-0.0189

V. Conclusion

A system identification procedure was developed based on the frequency response method outlined in [1] and tailored to the application of small, flying-wing UAS with only elevon controls. Configurable, automated frequency sweeps were used as control inputs to excite the longitudinal and lateral-directional UAS dynamics over a large range of frequencies. Adjusting control input parameters in real-time based on the UAS response, which was monitored via telemetry, ensured that the UAS responded with ample SNR and stayed near the trim condition. This resulted in high-quality flight data used for system identification. Low-order transfer functions were identified to provide initial parameter estimates and further verification of state space results. A simultaneous fitting procedure ensured the short-period parameters estimated from transfer functions matched well with those identified from the state space model results. Both the transfer function and state space models were identified with a high accuracy, as shown through the various performance metrics and comparison with doublet data. Finally, nondimensional stability and control derivatives were computed from the identified state space models for comparison with other aerodynamic modeling method. Monte Carlo simulation was employed to estimate the confidence intervals of these parameters.

Future results could be improved by collecting data with longer record times, which can lead to identification of lower frequency dynamics. This could be accomplished by modifying the procedure so that visual line-of-sight is not always necessary, such as through further automation of the procedure or through the use of first-person view systems. Additionally, collecting more flight data on calmer days could improve the SNR of the directional responses and improve the coherence and accuracy of the Dutch-roll mode identification. The results of this work can facilitate many other areas of research such as controller design, state estimator design, or turbulence encounter analysis. Future directions include extending the procedure to include thrust models and developing full-envelope dynamic models, which have a wider range of applicability than a state space model linearized at a single trim point.

Acknowledgements

This work is supported in part by the USDA-NIFA Grant 2019-67021-28992.

References

[1] Tischler, M., and Remple, R., *Aircraft And Rotorcraft System Identification: Engineering Methods With Flight-test Examples*, AIAA, Reston, VA, 2006.

[2] Klein, V., and Morelli, E., *Aircraft System Identification: Theory and Practice*, AIAA, Reston, VA, 2006.

[3] Jategaonkar, R. V., *Flight Vehicle System Identification: A Time-Domain Methodology, Second Edition*, AIAA, Reston, VA, 2015.

[4] Dorobantu, A., Murch, A., Mettler, B., and Balas, G., "System Identification for Small, Low-Cost, Fixed-Wing Unmanned Aircraft," *Journal of Aircraft*, Vol. 50, No. 4, 2013, pp. 1117–1130. https://doi.org/10.2514/1.C032065.

[5] Woodrow, P., Tischler, M., Mendoza, G., Hagerott, S. G., and Hunter, J., "Low Cost Flight-Test Platform to Demonstrate Flight Dynamics Concepts using Frequency-Domain System Identification Methods," *AIAA Atmospheric Flight Mechanics (AFM) Conference*, 2013. https://doi.org/10.2514/6.2013-4739.

[6] Sanders, F. C., Tischler, M., Berger, T., Berrios, M. G., and Gong, A., "System Identification and Multi-Objective Longitudinal Control Law Design for a Small Fixed-Wing UAV," *2018 AIAA Atmospheric Flight Mechanics Conference*, 2018. https://doi.org/10.2514/6.2018-0296.

[7] McGrail, A. K., "OnBoard Parameter Identification for a Small UAV," *West Virginia University Graduate Theses, Dissertations, and Problem Reports*, 2012. URL https://researchrepository.wvu.edu/etd/492.

[8] Simmons, B. M., McClelland, H. G., and Woolsey, C. A., "Nonlinear Model Identification Methodology for Small, Fixed-Wing, Unmanned Aircraft," *Journal of Aircraft*, Vol. 56, No. 3, 2019, pp. 1056–1067. https://doi.org/10.2514/1.C035160.

[9] Olsson, C., Verling, S. L., Stastny, T., and Siegwart, R., *Full Envelope System Identification of a VTOL Tailsitter UAV*, ???? https://doi.org/10.2514/6.2021-1054.

[10] Grymin, D. J., and Farhood, M., "Two-Step System Identification and Trajectory Tracking Control of a Small Fixed-Wing UAV," *Journal of Intelligent Robotic Systems*, Vol. 80, No. 1, 2015, pp. 105–131. https://doi.org/10.1007/s10846-015-0298-8.

[11] Flanagan, H. P., Hagerott, S. G., and Chao, H., "Model Based Roll Controller Tuning and Analysis for Small UAS in Turbulent Environments," *2018 International Conference on Unmanned Aircraft Systems (ICUAS)*, 2018, pp. 1398–1407. https://doi.org/10.1109/ICUAS.2018.8453442.

[12] Flanagan, H. P., Chao, H., and Hagerott, S. G., "Model Based Roll Controller Tuning and Frequency Domain Analysis for a Flying-Wing UAS," *2019 International Conference on Unmanned Aircraft Systems (ICUAS)*, 2019, pp. 721–728. https://doi.org/10.1109/ICUAS.2019.8798212.

[13] Smith, G., Bixler, B., Babcock, J. T., Osteroos, R., McLaughlin, T. E., and Tischler, M. B., "System Identification of the ICE/SACCON UAS Aircraft," *AIAA Scitech 2020 Forum*, 2020. https://doi.org/10.2514/6.2020-0289.

[14] Venkataraman, R., and Seiler, P., "System Identification for a Small, Rudderless, Fixed-Wing Unmanned Aircraft," *Journal of Aircraft*, Vol. 56, No. 3, 2019, pp. 1126–1134. https://doi.org/10.2514/1.C035141.

[15] McRuer, D., Ashkenas, I., and Graham, D., *Aircraft Dynamics and Automatic Control*, Princeton University Press, 1973.

[16] Berger, T., Tischler, M. B., Hagerott, S. G., Christopher Cotting, M., and Gray, W. R., "Identification of a Full-Envelope Learjet-25 Simulation Model Using a Stitching Architecture," *Journal of Guidance, Control, and Dynamics*, Vol. 43, No. 11, 2020, pp. 2091–2111. https://doi.org/10.2514/1.G005094.

[17] Beard, R. W., and McLain, T. W., *Small Unmanned Aircraft: Theory and Practice*, 1st ed., Princeton University Press, Princeton, NJ, 2012.

[18] Roskam, J., *Airplane Flight Dynamics & Automatic Flight Controls: Part I*, DARcorporation, Lawrence, KS, 1995.

[19] Gracey, W., "The Experimental Determination of the Moments of Inertia of Airplanes by a Simplified Compound-Pendulum Method," *NACA-TN-1629*, 1948.